ACS APPLIED MATERIALS & INTERFACES

www.acsami.org

Research Article

Alkynyl-Based Covalent Organic Frameworks as High-Performance Anode Materials for Potassium-Ion Batteries

Eric R. Wolfson,[‡] Luke Schkeryantz,[‡] Erica M. Moscarello, Joseph P. Fernandez, Jonah Paszek, Yiying Wu, Christopher M. Hadad, and Psaras L. McGrier*

Cite This: *ACS Appl. Mater. Interfaces* 2021, 13, 41628–41636

Read Online

ACCESS | Metrics & More | Article Recommendations | Supporting Information

ABSTRACT: The development of high-performance organic electrodes for potassium-ion batteries (KIBs) is attracting interest due to their sustainability and low costs. However, the electrolyte systems and moieties that generally proved to be successful in high-performance Li-ion batteries have found relatively little success in KIBs. Herein, two alkynyl-based covalent organic frameworks (COFs) containing 1,3,5-tris(arylethynyl)benzene (TAEB) and dehydrobenzoannulene (DBA) units are utilized as bulk anode materials for KIBs in a localized high-concentration electrolyte. TAEB-COF provides a high capacity value of 254.0 mAh g^{-1} at ∼100% efficiency after 300 cycles, and DBA-COF 3 provides a capacity of 76.3 mAh g^{-1} with 98.7% efficiency after 300 cycles. DFT calculations suggest that the alkynyl units of TAEB-COF facilitate the binding of K-ions through both enthalpic and geometric driving forces, leading to high reversible capacities.

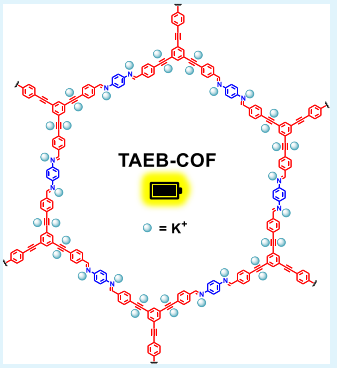

KEYWORDS: *covalent organic frameworks, alkynes, energy storage, potassium-ion batteries, organic electrodes*

1. INTRODUCTION

The persistent effort to reduce global warming by minimizing our dependence on fossil fuels has led to the development of many diverse energy storage systems.[1] The Li-ion battery (LIB) is perhaps the most popular high-performance energy storage system due to lithium's small atomic radius (0.68 Å), low redox potential (−3.04 V vs E^0), and low mass-to-charge ratio (6.94).[2−4] Although LIB technology has become ubiquitous in modern society as an essential power source for portable electronics, LIBs will eventually become an unsustainable long-term solution for expansive energy storage systems on account of lithium's high cost and limited availability.[5−7] As a consequence, potassium-ion batteries (KIBs)[8−10] are slowly emerging as a low-cost alternative to LIBs owing to the abundance of potassium (∼1.5%), a low standard redox potential (−2.93 V vs E^0) comparable to lithium, and faster ion transport kinetics in organic-based electrolytes.[11−13] The performance of a KIB is greatly influenced by the electrolyte and the anode materials that are used for its fabrication.[12,14,15] Typically, KIB assembly includes the use of a K^+ source with a carbonate-based organic solvent in either a low-concentration electrolyte or high-concentration electrolyte (HCE) system. Recently, Qin and co-workers demonstrated that a localized high-concentration electrolyte (LHCE) system made by diluting a high-concentration system with highly fluorinated ethers (HFEs) greatly improved the reversible capacity and cycling stability of graphite anodes in KIBs.[16] However, utilization of the LHCE system for other KIB anode materials remains greatly under-investigated, and there is great interest in developing organic-based electrode materials that can produce high-performance KIB systems.

Two major classes of electrode materials are inorganic and organic materials. Inorganic electrodes often comprise expensive and environmentally harmful metals. In addition, the common inorganic electrodes for K-ion batteries have relatively low capacities. For example, the commonly used Prussian blue cathode $[KFe^{III}Fe^{II}(CN)_6]$ has a reversible capacity of only ∼80 mA g^{-1}.[13,17−19] Functionalization of the material can be difficult depending on the metals utilized. Organic electrode materials provide several advantages over their inorganic counterparts. They traditionally contain abundant light elements (C, H, O, N, and S) with moderately inexpensive and environmentally friendly synthesis methods. Their structures can be more easily tuned and functionalized to help improve electrochemical performances. However, small organic molecules can dissolve in electrolyte solution, resulting in lower electrochemical performance.[20,21]

Received: June 10, 2021
Accepted: August 18, 2021
Published: August 27, 2021

Scheme 1. Synthetic Scheme for TABP-COF, TAEB-COF, and DBA-COF 3

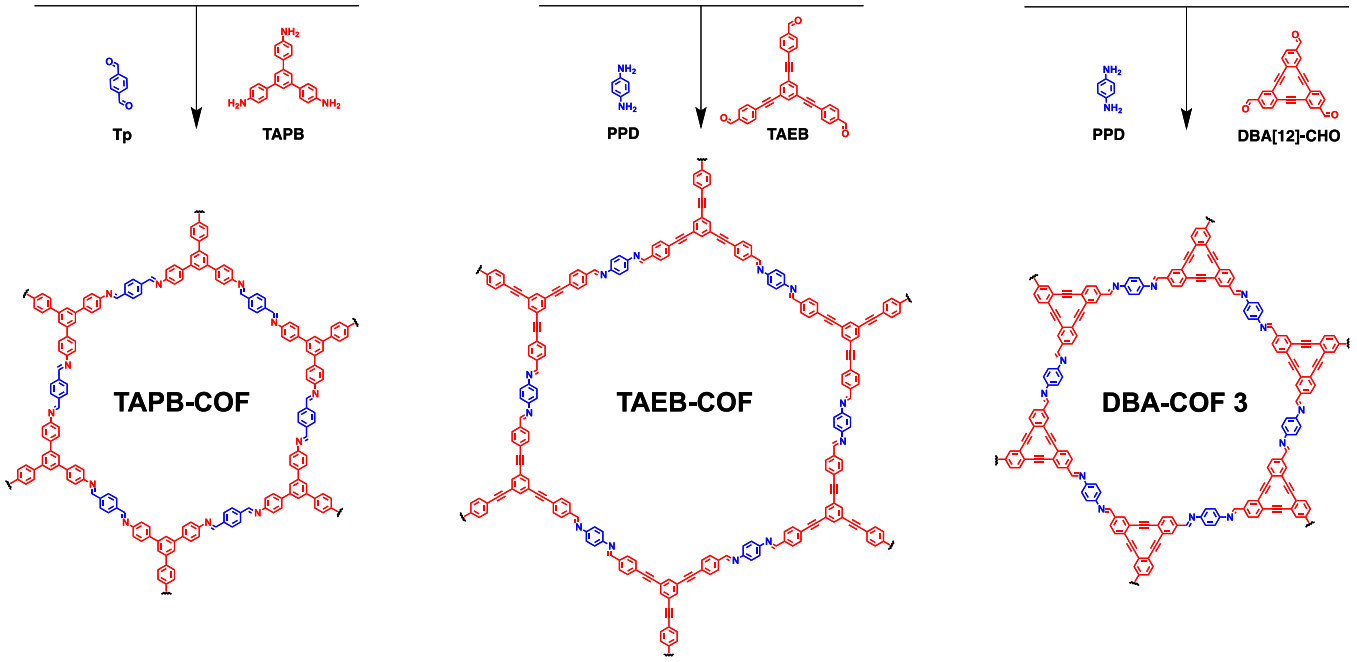

Covalent organic frameworks (COFs),[22−24] a crystalline class of porous materials, have become a suitable platform to construct organic electrodes for KIBs on account of their high surface areas, great chemical stability, and tunable pore sizes. These attributes make COFs beneficial for applications related to energy storage,[25,26] catalysis,[27,28] and chemical sensing.[24,29−31] Thus far, several COF-based systems have exhibited outstanding performance as electrode materials for LIBs due to their tunable molecular architectures.[32−34] However, examples of COF-based electrodes for KIBs are rare, and there are only a few reported systems. Recently, Chen and co-workers showed[35] that the boronate ester-linked COF-10 can be grafted onto carbon nanotubes (CNTs) and utilized as an anode material for KIBs.

Interestingly, the COF-10@CNT system produced a reversible capacity of 288 mAh g^{-1} after 500 cycles. However, when tested as a bulk material, COF-10 demonstrated a low reversible capacity of 57 mAh g^{-1} after 500 cycles. Although COFs may provide a good solution to improving KIB systems, examples of COFs capable of providing high performance without the need for filler materials would be advantageous.

Herein, we report the electrochemical performance of three imine-linked COFs containing 1,3,5-tris(4-aminophenyl)-benzene (TAPB),[36] 1,3,5-tris(arylethynyl)benzene (TAEB), and dehydrobenzoannulene (DBA)[37] units as anode materials for KIBs (Scheme 1). We show that TAEB-COF and DBA-COF 3, both of which contain alkynyl functional groups, exhibited initial capacities of 505 and 318 mAh g^{-1} and reversible capacities of 254 and 76 mAh g^{-1}, respectively, after 300 cycles at 50 mA g^{-1}. In contrast, TAPB-COF, which does not contain alkynyl groups, exhibited an initial capacity of 13 mAh g^{-1} and a low reversible capacity of ∼1 mAh g^{-1} after 300 cycles at 50 mA g^{-1}. The higher capacities for TAEB-COF and DBA-COF 3 are attributed to (1) the ability of the soft alkynyl ligands in each system to form significant cation−π interactions with K-ions during the potassiation/depotassiation process and (2) performance enhancement from an LHCE system composed of potassium bis(fluorosulfonyl)imide (KFSI) in ether- and HFE-based solvents. This work highlights the benefits of utilizing the combination of an LHCE system and alkynyl units to help improve the bulk performance of COF-based anode materials for KIBs.

2. EXPERIMENTAL SECTION

2.1. Chemicals and Materials. All reagents were purchased from commercial sources and used without further purification. Tetrahydrofuran and methanol were purified by passage over activated alumina.

KFSI (99.9%) was purchased from Fluolyte. 1,2-dimethoxyethane (DME) was purchased from BASF. 1,1,2,2-Tetrafluoroethyl-2,2,2-trifluoroethyl ether (TTE) was purchased from TCI. Both solvents were kept in separate bottles over 3 Å molecular sieves (Sigma-Aldrich) to maintain water content below 10 ppm. A glass fiber separator was purchased from Whatman. K metal (98%) was purchased from Sigma-Aldrich. Celgard (PP-PE-PP, 25 μm thickness), Cu foil (99.99%), cathode and anode casings, stainless steel spacers, and springs were purchased from the MTI corporation. All materials for electrochemical studies were stored and handled in an argon-filled glovebox (<0.5 ppm H_2O and <3.0 ppm O_2).

2.2. Instrumentation and Methods. Infrared spectra were recorded on a Thermo Scientific Nicolet iS5 with an iD7 diamond ATR attachment and are uncorrected, unless otherwise stated. ^{1}H NMR spectra were recorded in deuterated solvents on a Bruker Advance DPX 400 (400 MHz). Chemical shifts are reported in parts per million (ppm, δ) using the solvent as the internal standard. Solid-state ^{13}C NMR spectra for COF samples were recorded using a Bruker AVIII 600 MHz spectrometer with a wide-bore magnet (600.3 MHz) using a 3.2 mm magic angle spinning (MAS) HXY solid-state NMR probe and running 20 k scans. Cross-polarization with MAS (CP-MAS) was used to acquire ^{13}C data at 150.9 MHz. The ^{13}C cross-polarization time was 2 ms at 50 kHz with a 3 s relaxation delay for ^{13}C. ^{1}H decoupling was applied during data acquisition. The decoupling power was 100 kHz. The HXY sample spinning rate was 15 kHz. A 20 Hz line broadening was applied.

Surface area measurements were conducted on a Micromeritics ASAP 2020 Surface Area and Porosity Analyzer using ca. 15 mg samples. Nitrogen isotherms were generated by incremental exposure to ultrahigh purity nitrogen up to ca. 1 atm in a liquid nitrogen (77 K) bath. Surface parameters were determined using Brunauer−Emmett−

https://doi.org/10.1021/acsami.1c10870
ACS Appl. Mater. Interfaces 2021, 13, 41628−41636

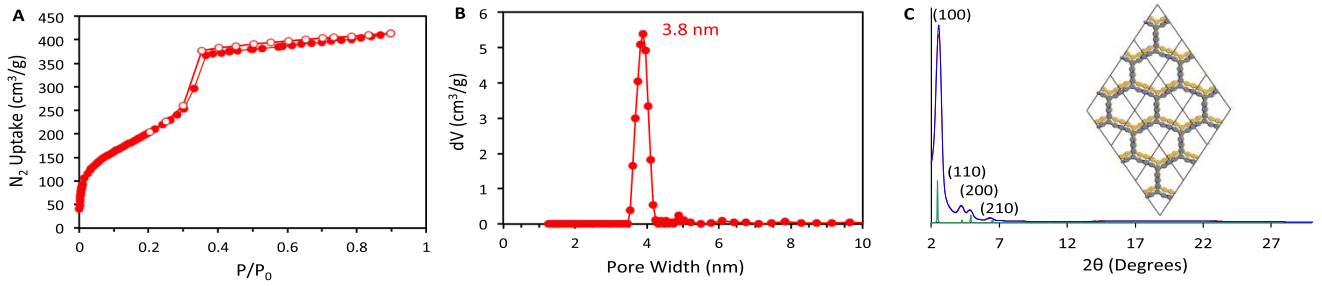

Figure 1. (A) Nitrogen adsorption/desorption isotherm at 77 K and (B) NLDFT pore size distribution for TAEB-COF. (C) Indexed experimental (red) and Pawley refined (blue) profiles of TAEB-COF overlaid with the simulated P6 hexagonal unit cell (green) offset by 5 Å.

Teller (BET) adsorption models in the instrument software. Pore size distributions were determined using the nonlocal density functional theory (NLDFT) model (cylindrical pore, N_2—cylindrical pores—oxide surface) in the instrument software (Micromeritics ASAP 2020 V4.02).

Scanning electron microscopy (SEM) was performed on a ThermoFisher Apreo field emission scanning electron microscope. The electrode samples were adhered to a sample holder using carbon sticky tape and imaged without any metal coating to preserve the morphology of potentially nanoscale features of interest. The powdered sample was deposited thinly by gently scraping material over the surface of a carbon sticky tab attached to an aluminum sample stub. The sample was imaged without any metal coating to preserve the morphology of potentially nanoscale features of interest. To mitigate image artifacts from sample charging, the SEM chamber was first pumped to high vacuum and then back-filled with 50 Pa of water vapor. A pressure-limiting aperture was attached to the pole piece to enable use of the Apreo's in-column voltage booster tube and electrostatic final lens features. The accelerating voltage was set to 1.3 kV, and images were collected using a low vacuum detector.

The COF electrodes were fabricated by mixing the appropriate COF powder, Super P carbon powder (MTI Corporation), and poly(vinylidenefluoride) (PVDF, Sigma-Aldrich) in *N*-methylpyrrolidone (Sigma-Aldrich) solvent. The slurry was then pasted onto the Cu foil (99.99%, 15.5 mm diameter, MTI) and dried at 70 °C for 12 h under vacuum. The loading amount is about 1.0 to 1.5 mg/cm^2 on each Cu substrate. The electrochemical process of K intercalation into each COF electrode was tested using CR2032-type coin cells, each of which consisted of a Cu foil (15.5 cm in diameter) as the working electrode, a trilayer celgard (polypropylene—polyethylene—polypropylene, 25 μm thickness), and a K chip (98%, Sigma-Aldrich) fabricated using an in-house process as the counter electrode. Fifty microlitersof the electrolyte is used in each cell. Galvanostatic cycling was performed in a K-COF half-cell between 0.05 and 3.0 V (vs K^+/K) at the rate of 50—500 mA/$g_{(COF\ active\ material)}$. The cycling was carried out using an MTI battery analyzer (BST8-WA).

Rate performance cycling was acquired by a Neware battery analyzer (BTS3000). After the first high capacity cycle, five cycles were performed at each rate from 50 to 2000 mA g^{-1} from 0.05 to 3 V vs K^+/K. Cyclic voltammograms for KIB coin cells were acquired using a Gamry Reference 600 Potentiostat/Galvanostat. Measurements were performed with a K-metal reference/counter electrode and a 60:30:10 COF:Super-P:PVDF electrode on a copper foil as the working electrode. LHCE was used as the supporting electrolyte. A sweep rate of 10 mV s^{-1} was used. The sweep rate dependence experiments to determine faradaic/capacitative redox were run on a Bio-Logic SP-150 potentiostat. The coin cell was swept from 0.05 to 2 V vs K^+/K under varying sweep rates.

Electrochemical impedance spectroscopy (EIS) was acquired with a Gamry Reference 600 Potentiostat/Galvanostat. Impedance measurements were run from 1 MHz to 0.1 Hz with 10 points per decade and an applied AC voltage of 10 mV. X-ray photoelectron spectroscopy (XPS) was carried out on a Kratos Axis Ultra X-ray photoelectron spectrometer. The pristine electrode was measured as prepared. The potassiated electrode was cycled at 50 mA g^{-1} for one full cycle from 0.05 to 3 V vs K^+/K and then discharged one additional time. The depotassiated electrode was cycled for one full cycle and discharged and then charged one additional time. Electrodes were transferred into the XPS instrument using an air-free sample holder. C 1s spectra were acquired over eight sweeps.

Thermogravimetric analysis (TGA) was performed on a Discovery TGA 550 using a ramp rate of 5 °C/min from room temperature to 1000 °C under nitrogen gas. Elemental analysis was performed by Galbraith Laboratories.

2.3. Preparation of the TAEB Monomer. Under an Ar atmosphere, an oven-dried round-bottom flask equipped with a stirrer bar was charged with 1,3,5-tribromobenzene (1.44 g, 4.57 mmol, 1.0 equiv), $PdCl_2(PPh_3)_2$ (323 mg, 0.092 mmol, 0.1 equiv), copper iodide (175 mg, 0.92 mmol, 0.2 equiv), triphenylphosphine (241 mg, 0.92 mmol, 0.2 equiv), and 4-ethynylbenzaldehyde (2.50 g, 19.2 mmol, 4.2 equiv). The flask was capped with a septum and transferred to a condenser. Degassed triethylamine (100 mL) was added by a syringe. The resulting suspension was heated at reflux overnight before being allowed to cool to ambient temperature. The reaction was diluted with water (150 mL), and the solid was collected by filtration, washed with water, and dried on the filter. The resulting solid was purified via column chromatography (0—10% EtOAc in DCM), and the product containing fractions was concentrated to ~25 mL. The EtOAc suspension was filtered, and the solid was washed with further EtOAc before it was dried in vacuo to afford the desired product 25 as a colorless solid (1.50 g, 3.2 mmol, 71%). ^{1}H NMR (400 MHz, $CDCl_3$): δ 10.04 (3 H, s), 7.90 (6 H, d), 7.74 (3 H, s), 7.69 (6 H, d); ^{13}C NMR (100 MHz, $CDCl_3$): δ 191.5, 136.0, 135.0, 132.4, 129.8, 128.9, 123.8, 91.3, 90.1 ppm.

2.4. Preparation of TAEB-COF. TAEB (43.9 mg, 0.095 mmol, 1 equiv) and *p*-phenylenediamine (20 mg, 0.14 mmol, 1.5 equiv) were combined in a 4 mL dram. The solids were suspended in 1 mL of a 4:1 solution of 1,4-dioxane/mesitylene and sonicated for 1 min. The suspension was heated to 70 °C until all solids dissolved, and then acetic acid (0.5 mL, 10.5 M) was added dropwise. The vial was capped and gently swirled before heating for 24 h at 70 °C. The vial was removed from heat, cooled to room temperature, and filtered with 3 × 15 mL washes of dry MeOH. The solids were then solvent-exchanged in dry MeOH over 24 h before activating under nitrogen flow at 120 °C to provide TAEB-COF (47.7 mg, 88% yield) as a bright yellow fluffy powder.

2.5. Preparation of TAPB-COF and DBA-COF 3. TAPB-COF[36] and DBA-COF 3[37] were obtained by using synthetic protocols that have been previously reported.

3. RESULTS AND DISCUSSION

3.1. Characterization of TAEB-COF. TAEB-COF was characterized using Fourier transform infrared spectroscopy (FT-IR) and CP-MAS spectroscopy. The FT-IR spectra disclosed stretching modes for the imine groups at 1610 cm^{-1} and the alkynyl units at 2150 cm^{-1} (Figure S13). The structure of TAEB-COF was confirmed by ^{13}C CP-MAS exhibiting resonances at 154.8 and 89.2 ppm, which correspond to the imine linkage and alkynyl units, respectively

https://doi.org/10.1021/acsami.1c10870
ACS Appl. Mater. Interfaces 2021, 13, 41628—41636

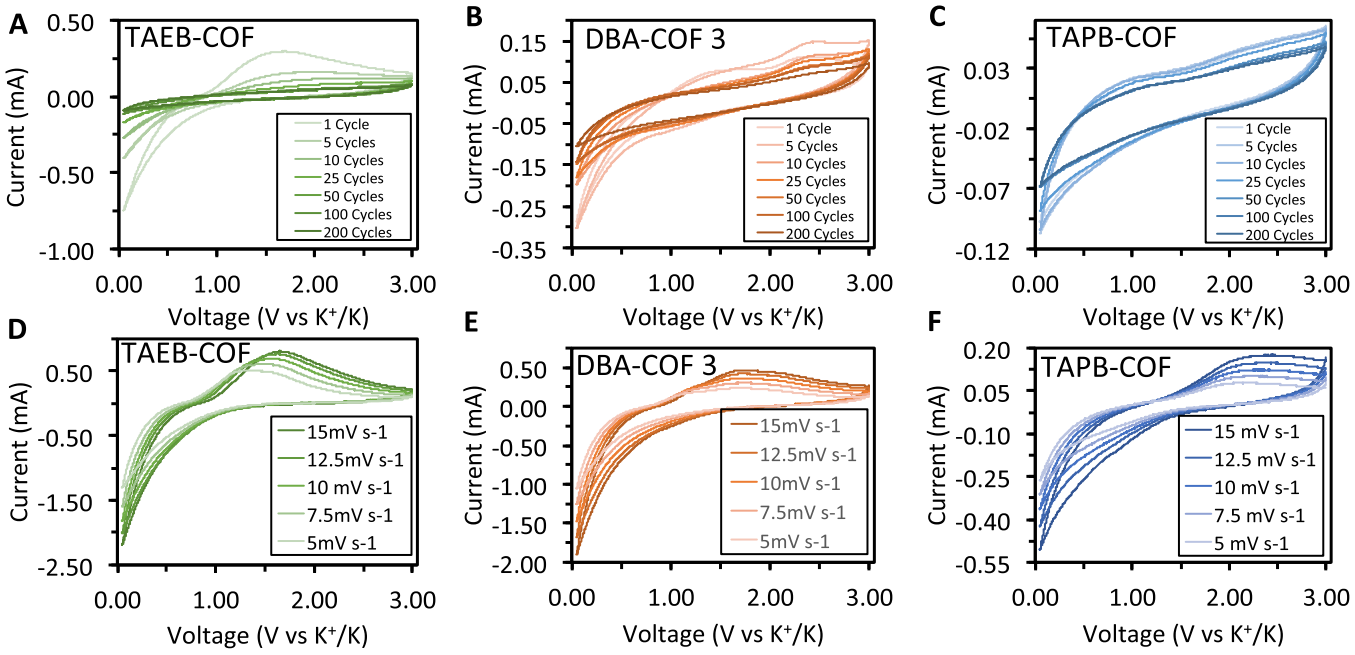

Figure 2. (A–C) Cyclic voltammograms of the COFs swept from 0.05 and 3 V vs K^+/K at 10 mV s^{-1} after 200 cycles. Cyclic voltammograms run at the fully charged state (3 V vs K^+/K) after the indicated number of cycles. (D–F) Variable sweep rate cyclic voltammetry (CV) investigation for all three systems with (inset) the linear relationship between max/min peak current vs the square root of the scan rate. Scans performed from 5 to 15 mV s^{-12}.

(Figure S14). TGA revealed that TAEB-COF maintained ~90% of its mass up to a temperature of 490 °C (Figure S1). SEM images exhibited the formation of feathery crystallites (Figure S2).

The porosity of TAEB-COF was assessed using nitrogen gas adsorption (Figure 1A). TAEB-COF exhibited a type IV isotherm, revealing a rapid uptake at low pressures (P/P_0 < 0.1) and another surge in uptake at higher pressure (0.3 < P/P_0 < 0.4). Applying the BET model over the low-pressure region (0.1 < P/P_0 < 0.3) afforded a surface area of 816 m^2 g^{-1}. The total pore volume calculated at P/P_0 = 0.898 provided a value of 0.64 cm^3 g^{-1}. Estimation of the pore size distribution using the NLDFT method revealed an average pore size of 3.8 nm for TAEB-COF (Figure 1B). Surprisingly, the experimental pore size is slightly lower than the theoretical value of 4.3 nm, suggesting that the layers are offset by ~0.5 nm. The surface areas and pore sizes of DBA-COF 3 and TAPB-COF were comparable to the previously reported values (Figures S5–S8).

The crystallinity of TAEB-COF was assessed utilizing powder X-ray diffraction (PXRD) measurements. Taking into account the differences between theoretical and experimental pore sizes of TAEB-COF, the structure was modeled using a P6 hexagonal unit cell and offsetting the layers by 5 Å (Figure 1C). TAEB-COF displays an intense peak at 2.40° along with smaller peaks at 4.16, 4.80, and 6.36°, which correspond to the (100), (110), (200), and (210) peaks, respectively. Pawley refinement of the experimental data yielded unit cell parameters of $a = b$ = 42.448 Å and c = 3.4 Å (residuals R_p = 2.95%, R_{wp} = 3.60%). The simulated pattern overlapped well with the experimental plot. The PXRD profiles of DBA-COF 3 and TAPB-COF were consistent with previously reported patterns (Figures S11 and S12).

3.2. Electrochemical Performance. The CV measurements for TAEB-COF, DBA-COF 3, and TAPB-COF were taken in their pristine state using an LHCE system comprising 2.76 molal (m) KFSI in DME diluted with TTE in a 2:1 ratio (Figure 2A–C). TAEB-COF displayed a broad reduction peak at 1.4 V (between 0.05 to 3.0 V) that gradually decreases after the first 25 cycles due to the partial reduction and subsequent oxidation of the electrolyte, resulting in the formation of the solid electrolyte interface (SEI) layer. Interestingly, DBA-COF 3 demonstrated similar electrochemical behavior but at a lower overall current, which corresponds to less intercalation of potassium ions. The large current response, including the broad peaks at 1.4 and 2.4 V, in the initial cycles is likely due to SEI formation and partial reoxidation. In contrast to TAEB-COF and DBA-COF 3, TAPB-COF exhibits reduction peaks that are much lower in intensity and the lack of large peaks in the initial cycles indicates insufficient growth of the SEI layer. We believe that this is due to the lack of potassium intercalation into the material as a result of insufficient, inactive, or unaccommodating potassiation sites. The peak currents for TAEB-COF and DBA-COF 3 increase linearly with the square root of the sweep rate, which indicates that the redox kinetics of both systems are faradaic (Figures 2D,E). In contrast, the peak currents for TAPB-COF display a nonlinear relationship, which is indicative of a capacitive electrochemical process.

In an effort to find the most suitable LCHE system for optimal device performance, charge/discharge cycling at a current loading of 50 mA g^{-1} was used to optimize the electrolyte composition for TAEB-COF during battery cycling (Figure 3A). Initial tests using carbonate-based electrolyte systems such as 0.87 KFSI in ethylene carbonate (EC)/dimethyl carbonate (DMC) displayed poor performance with charge capacities below 10 mAh g^{-1} after 100 cycles. However, it is known that ether-based electrolytes like DME can enhance performance in KIBs compared to EC/DMC by discouraging the decomposition of the electrolyte and providing a thinner solid SEI layer.[38] Additionally, K^+-solvent co-intercalation has

https://doi.org/10.1021/acsami.1c10870
ACS Appl. Mater. Interfaces 2021, 13, 41628–41636

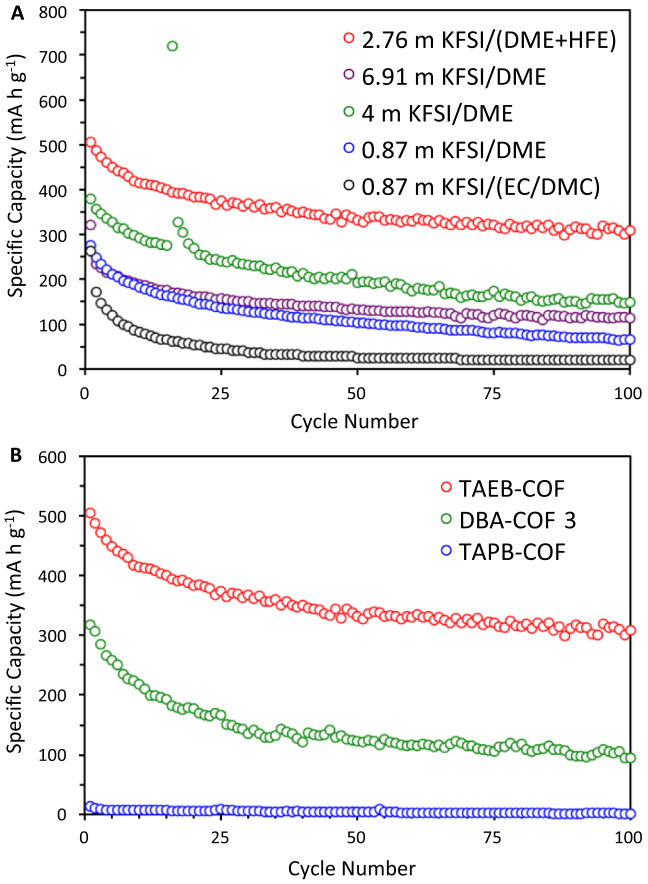

Figure 3. (A) Charge capacities for a TAEB-COF KIB coin cell at 50 mA g^{-1} fabricated using different electrolyte formulations. (B) Charge capacities for TAEB-COF, DBA-COF 3, and TAPB-COF using 2.76 m KFSI in DME and the HFE-based solvent TTE.

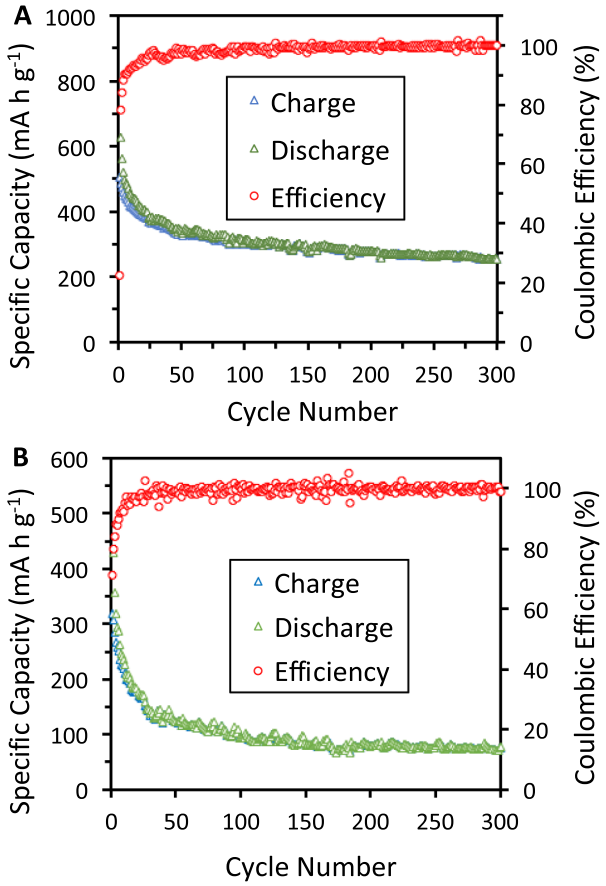

Figure 4. Cycling performances for (A) TAEB-COF and (B) DBA-COF 3 at 50 mA g^{-1} after 300 cycles using 2.76 m KFSI in DME and TTE.

been shown to readily occur in KIBs assembled with ether-based solvents, resulting in large (12.1 Å) interlayer spacings to accommodate the complexes.[39] In high concentrations of salt/solvent, these large interlayer spacings created via co-intercalation also greatly enhanced the diffusion coefficient of K^+-solvent complexes through graphite compared to Li^+ or Na^+. Thus, when an equal concentration of KFSI in DME was used as the electrolyte, the charge capacity increased to 66 mAh g^{-1} and early capacity fading was visibly reduced. Increasing the KFSI concentration to 4 m improved charge capacity further to 149 mAh g^{-1}; however, a subsequent increase to 6.91 m afforded a decrease in performance to 114 mAh g^{-1}. The former increase is likely due to greater availability of K^+ in solution, while the latter decrease could be attributed to increased viscosity, leading to poorer ionic conductivity, which is consistent with performance issues often seen in HCEs.[11] However, when an LHCE system comprising 2.76 m KFSI in DME diluted with TTE was used, the performance of the TAEB-COF dramatically improved to 308 mAh g^{-1}. In contrast, DBA-COF 3 yielded a charge capacity of 103 mAh g^{-1} after 100 cycles (Figure 3B). Surprisingly, the TAPB-COF system was essentially inactive and the optimal LCHE electrolyte formulation did not enhance the charge performance.

The cycling performances of TAEB-COF and DBA-COF 3 after 300 cycles at 50 mA g^{-1} are revealed in Figure 4.[40] The initial charge capacities for TAEB-COF and DBA-COF 3 afforded values of 505.4 and 318.0 mAh g^{-1}, respectively, when cycled at 50 mA g^{-1}. It should be noted that these initial capacity values are the highest values that have been reported for a metal-free KIB organic-based anode material at 50 mA g^{-1}. After 300 cycles, TAEB-COF exhibited a high reversible capacity of 254 mAh g^{-1} retaining 50% of its initial charge capacity, while yielding a coulombic efficiency of 99%. The reversible charge capacity value for TAEB-COF is on par with or higher than COF-10@CNT (288 mAh g^{-1}) and CTF-0 (113 mAh g^{-1}).[35,41] In contrast, DBA-COF 3 displayed a reversible capacity of 76.3 mAh g^{-1}, retaining 24% of its initial charge capacity, while yielding a coulombic efficiency of 98.7%. The capacity fading for both systems could be attributed to the emergence of irreversible K-ion binding sites on account of the creation of unstable SEI layers. TAPB-COF provided the lowest values exhibiting an initial capacity of 13 mAh g^{-1} and a reversible capacity of ∼1 mAh g^{-1} after 300 cycles at 50 mA g^{-1} (Figure S20). In addition to the charge/discharge measurements, we also investigated the rate performance of TAEB-COF and DBA-COF 3 (Figure 5A). Testing TAEB-COF at increasing densities of 50, 100, 150, 250, 500, 1000, and 2000 mA g^{-1} at five cycles each yielded reversible capacities of 395, 339, 298, 240, 169, 46, and 2 mAh g^{-1}, respectively. After the current density returned to 50 mA g^{-1}, the reversible capacity of TAEB-COF increased dramatically to 337 mAh g^{-1}, recovering more than 85% of its initial performance. In contrast, testing DBA-COF 3 at increasing densities of 50, 100, 150, 250, 500, 1000, and 2000 mA g^{-1} at

https://doi.org/10.1021/acsami.1c10870
ACS Appl. Mater. Interfaces 2021, 13, 41628−41636

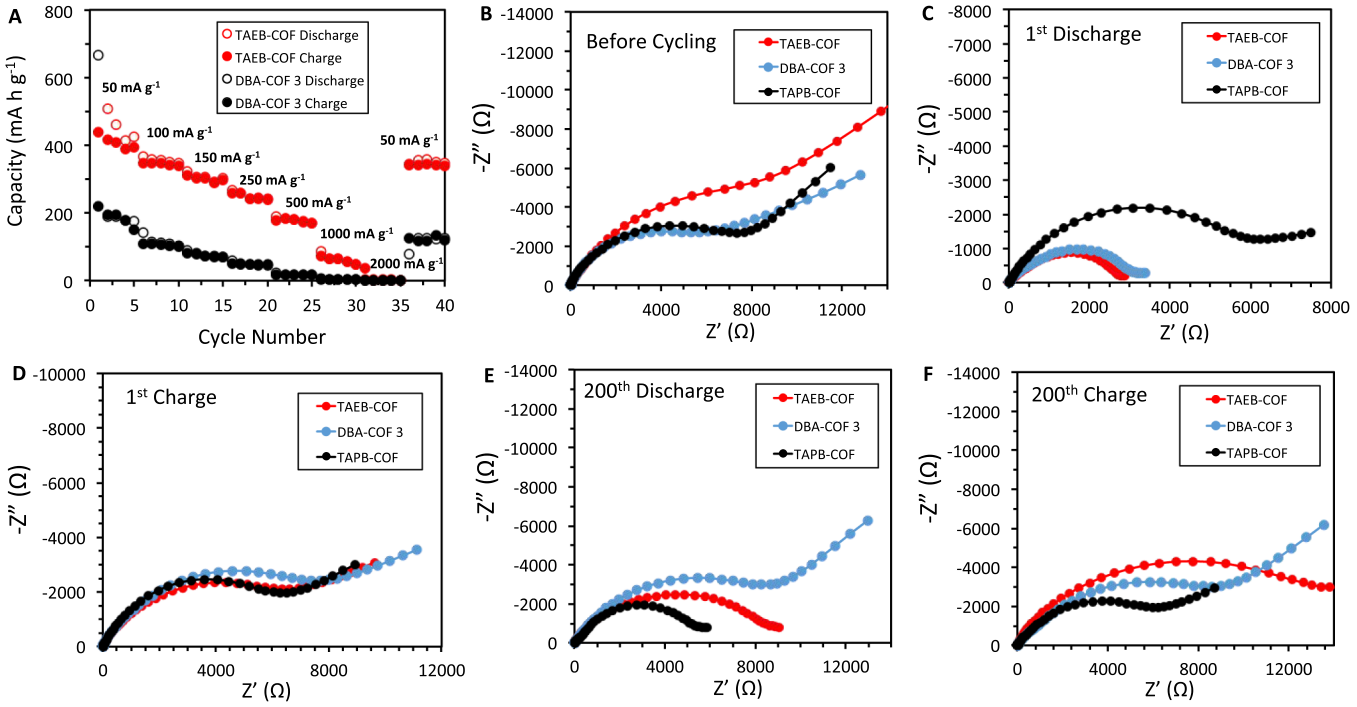

Figure 5. (A) Rate performance of TAEB-COF and DBA-COF 3 at different charge/discharge rates from 50 to 2000 mA g^{-1} at 5 cycles each. (B–F) EIS profiles for TAEB-COF, DBA-COF 3, and TAPB-COF before cycling and after the 1st and 200th charge/discharge cycles.

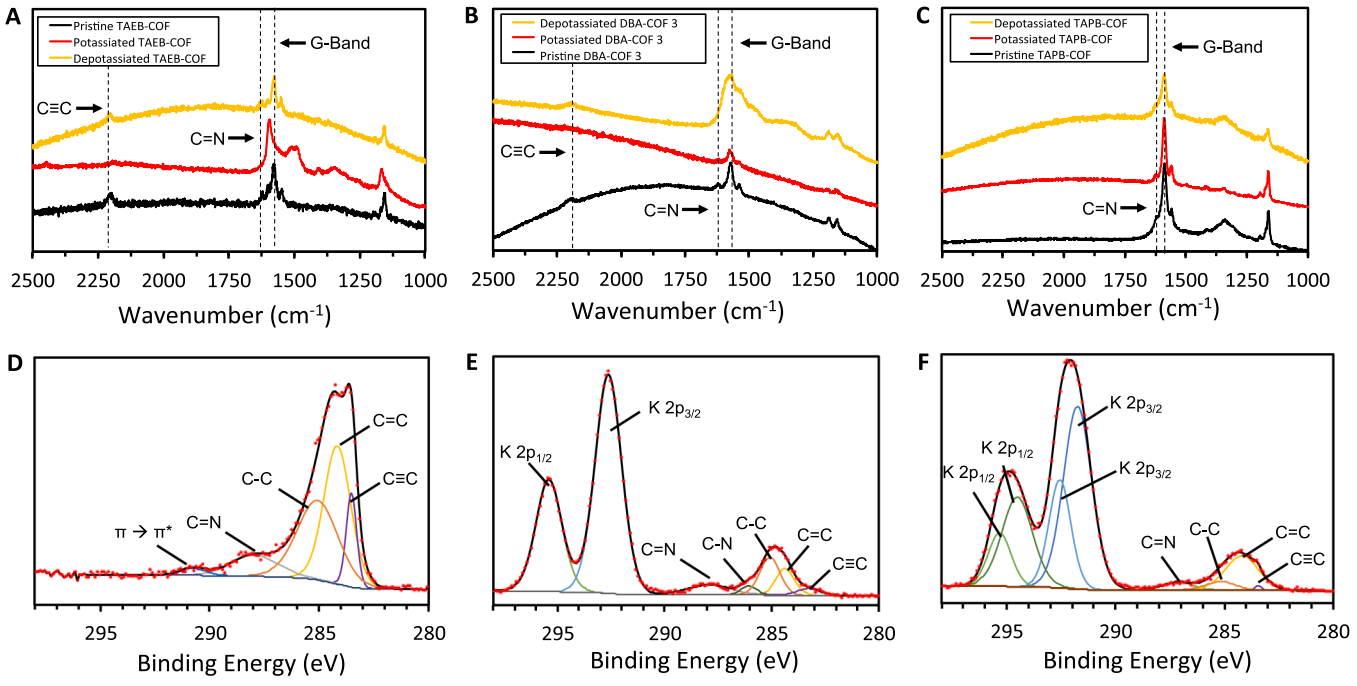

Figure 6. Raman spectra of (A) TAEB-COF, (B) DBA-COF 3, and (C) TAPB-COF in their pristine, potassiated, and depotassiated states. Deconvoluted XPS spectra of TAEB-COF in its (D) pristine, (E) potassiated, and (F) depotassiated states.

five cycles each yielded reversible capacities of 178, 104, 71, 46, 17, 4, and 1 mAh g^{-1}, respectively. After the current density returned to 50 mA g^{-1}, the reversible capacity of DBA-COF 3 increased to 120 mAh g^{-1}, recovering more than 65% of its initial performance.

EIS measurements of each COF system were taken before cycling and at their initial charged (3 V vs K^+/K)/discharged (0.05 V vs K^+/K)/ states (Figure 5B–F). The EIS profiles for DBA-COF 3 and TAPB-COF taken before cycling display a similar interfacial impedance, while the TAEB-COF exhibits a higher impedance value (Figure 5B). After the first discharge, the impedance values of the TAEB-COF and DBA-COF 3 decreased dramatically, while the impedance of TAPB-COF decreased slightly (Figure 5C). The reduction in impedance was more substantial for TAEB-COF (~7000 Ω) compared to DBA-COF 3 (~4000 Ω), which indicates that the free alkynyl moieties of TAEB-COF could be more adaptive to volume expansion during the potassiation process than the DBA

https://doi.org/10.1021/acsami.1c10870
ACS Appl. Mater. Interfaces 2021, 13, 41628–41636

macrocyclic units of DBA-COF 3. We believe the modest impedance reduction of TAPB-COF (~2000 Ω) is exclusively due to SEI formation during the discharge process. After the first charge, all three COF systems exhibited increased impedance values with TAPB-COF, displaying the most modest increase (Figure 5D). The minimal change for TAPB-COF is likely due to the dominant capacitive nature of the material. However, the overall increase for each COF system is likely attributed to the deintercalation of the potassium ions, which greatly expands the COF layers. As a consequence, this expansion reduces electrode contact with the current collector and lowers the conductivity of the system. After 200 cycles the impedance of the TAEB-COF and DBA-COF 3 significantly increased in the discharged and charged states (Figure 5E,F). This is likely due to continued growth of the SEI layers and pulverization of the COF material through continuous intercalation and deintercalation of K-ions.[32] This pulverization process can be observed by comparing SEM images of TAEB-COF electrodes before cycling and after potassiation/depotassiation (Figure S17).

To examine the potassiation/depotassiation process, we performed in situ Raman spectroscopy on the pristine, potassiated, and depotassiated coin cells of TAEB-COF and DBA-COF 3 (Figure 6A,B). TAEB-COF and DBA-COF 3 displayed alkynyl peaks at 2193 and 2211 cm^{-1}, respectively, which were sequestered after potassiation. These data indicate that the alkynyl units are potassiated during the cycling process. Upon depotassiation, the intensity of the alkynyl peaks in both cases is restored, indicating that both systems exhibit a high degree of reversibility. In addition, the G band (1580 cm^{-1}) of TAEB-COF undergoes significant attenuation followed by simultaneous growth of a large D′ band (1598 cm^{-1}), indicating that a large degree of disorder is induced by cation-π interactions between the sp^2 carbons of the benzene rings and K-ions throughout the layered stacks. However, depotassiation restores the intensities of both peaks, demonstrating the robust nature of TAEB-COF's bulk structure during cycling. Subsequent depotassiation of DBA-COF 3 results in broad peaks in the D band region. We believe that the broadening of the peaks suggests that the K-ion intercalation process is irreversible or the process simply promotes the disruption of the COF structure. In contrast, TAPB-COF shows no significant changes to the G band during potassiation, suggesting very little K-ion intercalation into the bulk structure (Figure 6C). The Raman spectra suggest that the non-macrocyclic alkynyl units of TAEB-COF promote the reversible volume expansion necessary during K^+ intercalation compared to TAPB-COF and DBA-COF 3. This could be due to the unique ability of alkynyl units of TAEB-COF to undergo conformational flexibility during volume expansion without compromising the high degree of $\pi-\pi$ stacking interactions necessary to facilitate the cycling process.[42−44] In contrast, due to its macrocyclic structure, sequential potassiation of DBA-COF 3 could induce puckering of the DBA core, disrupting planarity and discouraging subsequent potassiation events.

To further probe the K^+ storage mechanism of TAEB-COF, XPS was performed on pristine, potassiated, and depotassiated TAEB-COF coin cells. The C 1s region of the pristine coin cell exhibited five peaks at 290.7, 287.9, 285.0, 284.0, and 283.5 eV, which correspond to the C−N, C−C, C═C, and C≡C functional groups (Figure 6D). After potassiation, TAEB-COF shows a significant attenuation of both the C≡C and C═C peaks and simultaneous growth of the C−C peak, suggesting significant potassiation of the benzene and alkynyl units during the charge process (Figure 6E). Additionally, three new peaks emerge at 294.2, 291.6, and 286.0 eV corresponding K $2p_{1/2}$, K $2p_{3/2}$, and C−N, respectively. The emergence of the C−N peak at 286 eV could be attributed to potassiation of the imine groups during the discharge process. Depotassiation revealed the growth of a second set of peaks at 294.4 and 291.6 eV corresponding to the second potassium species generated, which is consistent with the formation of a robust SEI layer on the surface of the electrode (Figure 6F).[45] Interestingly, depotassiation effectively restores the C═C and C≡C peaks; however, the C≡C does not recover to its initial intensity, which could account for the lower coulombic efficiency values observed during the early charge/discharge cycles.

To better comprehend the binding interactions of K-ions with the alkynyl units of TAEB-COF and DBA-COF 3, we performed DFT calculations using TAEB-PI and DBA-PI, imine-linked precursors of TAEB-COF and DBA-COF 3, respectively (Figure S28). For TAEB-PI, we examined how three potassium ions could interact with one of the alkynyl units by exploring a combinatoric variety of geometries. In doing so, 11 structures were fully optimized to provide relative free energies ranging from 0 to 12 kcal/mol (Table S4). Interestingly, the potassium ions moved to locations above or below the plane of the ring, and no optimized geometry was found in which the potassium ions were coplanar to the rings. Several of the different starting geometries converged into local minima. Most noticeably, a C_2K_2 motif was observed in many of the optimized structures, where significant deviations from the linear sp. alkynyl carbon bond angle were observed. In the lowest energy structure, a C−C−C angle was observed to be 136°, a nearly 50° difference from the expected 180° (Figure 7). It should be noted that the K-ions appear to have a shared

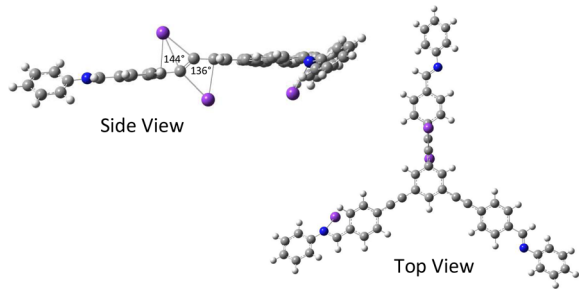

Figure 7. Visualization of optimized geometry (B4) of three potassium ions bound to radical anionic TAEB-PI. Deviation from the linear alkynyl bond (C−C−C) is shown in degrees.

interaction between the ipso-carbon of the phenyl ring and the carbon of the alkynyl unit. Other calculated structures revealed similar perturbations in both the geometry and vibrational frequencies of these C_2K_2 units (Figures S34−S40).

In addition, we attempted to produce saturated monomers utilizing the initial specific capacitance values of 505 and 318 mAh g^{-1} for TAEB-COF and DBA-COF 3, respectively. Interestingly, the calculations show that the TAEB-PI monomer can bind 10 K-ions, while the DBA-PI monomer can bind 5. Two optimized minima were found with 10 K-ions bound to TAEB-PI, which exhibited a similar structure and vibrational features, as described for the 3 K-ion systems (Figures S41 and S42). While a structure with five bound potassium ions for DBA-PI was found, it did not exhibit the

https://doi.org/10.1021/acsami.1c10870
ACS Appl. Mater. Interfaces 2021, 13, 41628−41636

analogous alkynyl interactions, suggesting that these interactions could be influenced by the macroscopic geometry of the COF structure (Figure S44). However, a structure with four bound K-ions was found for DBA-PI, which exhibited the C_2K_2 motif, showing that the sort of alkynyl perturbation observed for TAEB is also possible for the DBA-COF 3. In contrast, the lack of alkynyl units in the TAPB monomer prevents any additional binding of potassium beyond the single observed aryl ring cation−π interaction.

Overall, these features in the C_2K_2 motifs for TAEB-COF and DBA-COF 3 imply that the alkynyl units do indeed play a significant role in facilitating the binding of the potassium ions. The differences in the specific capacity values are likely due to the geometric constraints of the monomers. In particular, the extended linear structure and conformational flexibility of the alkynyl units in the TAEB linker affords a large space to accommodate more intercalating K-ions. In contrast, the condensed ring structure of the DBA alkynyl units allow for less K-ion intercalation.

4. CONCLUSIONS

In summary, we have showed that alkynyl-based COFs can be utilized as efficient KIB electrodes in the bulk phase in the presence of an LHCE system. TAEB-COF and DBA-COF 3 exhibited initial capacities of 505 and 318 mAh g^{-1} and reversible capacities of 254 and 76 mAh g^{-1}, respectively, after 300 cycles at 50 mA g^{-1}, utilizing the LHCE system. Although both COFs were able to use their alkynyl ligands to facilitate significant cation−π interactions with K-ions during the potassiation/depotassiation process, the TAEB-COF exhibited the best K-ion storage capacity due to its ability to accommodate the intercalation of K-ions on account of the conformational flexibility of the TAEB linkers. This work highlights the benefits of using alkynyl-based COFs and an LHCE system to construct high-capacity electrodes for KIBs. Such investigations could be fruitful in developing battery technology that is sustainable and capable of meeting long-term energy storage demands.

■ ASSOCIATED CONTENT

Supporting Information

The Supporting Information is available free of charge at https://pubs.acs.org/doi/10.1021/acsami.1c10870.

Experimental details, COF characterization, electrolyte optimization, and DFT calculations (PDF)

■ AUTHOR INFORMATION

Corresponding Author

Psaras L. McGrier − *Department of Chemistry and Biochemistry, The Ohio State University, Columbus, Ohio 43210, United States;* orcid.org/0000-0001-7637-4349; Email: mcgrier.1@osu.edu

Authors

Eric R. Wolfson − *Department of Chemistry and Biochemistry, The Ohio State University, Columbus, Ohio 43210, United States*

Luke Schkeryantz − *Department of Chemistry and Biochemistry, The Ohio State University, Columbus, Ohio 43210, United States*

Erica M. Moscarello − *Department of Chemistry and Biochemistry, The Ohio State University, Columbus, Ohio 43210, United States*

Joseph P. Fernandez − *Department of Chemistry and Biochemistry, The Ohio State University, Columbus, Ohio 43210, United States*

Jonah Paszek − *Department of Chemistry and Biochemistry, The Ohio State University, Columbus, Ohio 43210, United States*

Yiying Wu − *Department of Chemistry and Biochemistry, The Ohio State University, Columbus, Ohio 43210, United States;* orcid.org/0000-0001-9359-1863

Christopher M. Hadad − *Department of Chemistry and Biochemistry, The Ohio State University, Columbus, Ohio 43210, United States*

Complete contact information is available at: https://pubs.acs.org/10.1021/acsami.1c10870

Author Contributions

‡E.R.W. and L.S. contributed to this work equally.

Notes

The authors declare no competing financial interest.

■ ACKNOWLEDGMENTS

P.L.M. acknowledges financial support from the National Science Foundation (CBET-2037707). We thank The Ohio State University (OSU) Campus Chemical Instrument Center (CCIC) and Tanya Whitmer for assistance with the CP-MAS NMR measurements and access to the instrumentation. Electron microscopy was performed at the Center for Electron Microscopy and Analysis (CEMAS) at OSU. We also thank Dr. Yehia Khalifa and Songwei Zhang for assistance with the XPS measurements. J.P.F. and C.M.H. gratefully acknowledge access to the computational resources at the Ohio Supercomputer Center.

■ REFERENCES

(1) Koohi-Fayegh, S.; Rosen, M. A. A Review of Energy Storage Types, Applications and Recent Developments. *J. Energy Storage* **2020**, *27*, No. 101047.

(2) Kim, T.; Song, W.; Son, D.; Ono, L. K.; Qi, Y. Lithium-Ion Batteries: Outlook on Present, Future, and Hybridized Technologies. *J. Mater. Chem. A* **2019**, *7*, 2942−2964.

(3) Ji, H.; Wu, J.; Cai, Z.; Liu, J.; Kwon, D.; Kim, H.; Urban, A.; Papp, J. K.; Foley, E.; Tian, Y.; Balasubramanian, M.; Kim, H.; Clément, R. J.; McCloskey, B. D.; Yang, W.; Ceder, G. Ultrahigh Power and Energy Density in Partially Ordered Lithium-Ion Cathode Materials. *Nat. Energy* **2020**, *5*, 213−221.

(4) Seh, Z. W.; Sun, Y.; Zhang, Q.; Cui, Y. Designing High-Energy Lithum−Sulfur Batteries. *Chem. Soc. Rev.* **2016**, *45*, 5605−5634.

(5) Grosjean, C.; Miranda, P. H.; Perrin, M.; Poggi, P. Assessment of World Lithium Resources and Consequences of Their Geographic Distribution on the Expected Development of the Electric Vehicle Industry. *Renew. Sustain. Energy Rev.* **2012**, *16*, 1735−1744.

(6) Kushnir, D.; Sandén, B. A. The Time Dimension and Lithum Resource Constraints for Electric Vehicles. *Resour. Policy* **2012**, *37*, 93−103.

(7) Vikström, H.; Davidsson, S.; Hök, M. Lithium Availability and Future Production Outlooks. *Appl. Energy* **2013**, *110*, 252−266.

(8) Xie, J.; Li, X.; Lai, H.; Zhao, Z.; Li, J.; Zhang, W.; Xie, W.; Liu, Y.; Mai, W. A Robust Solid Electrolyte Interphase Layer Augments the Ion Storage Capacity of Bimetallic-Sulfide-Containing Potassium-Ion Batteries. *Angew. Chem., Int. Ed.* **2019**, *58*, 14740−14747.

(9) Li, J.; Zhuang, N.; Xie, J.; Li, X.; Zhuo, W.; Wang, H.; Na, J. B.; Li, X.; Yamauchi, Y.; Mai, W. K-Ion Storage Enhancement in Sb_2O_3/

Reduced Graphene Oxide Using Ether-Based Electrolyte. *Adv. Energy Mater.* **2020**, *10*, No. 1903455.
(10) Xie, J.; Li, J.; Li, X.; Lei, H.; Zhuo, W.; Li, X.; Hong, G.; Hui, K. N.; Pan, L.; Mai, W. Ultrahigh "Relative Energy Density" and Mass Loading of Carbon Cloth Anodes for K-Ion Batteries. *CCS Chem.* **2020**, *2*, 791−799.
(11) Hosaka, T.; Kubota, K.; Hameed, A. S.; Komaba, S. Research Development on K-Ion Batteries. *Chem. Rev.* **2020**, *120*, 6358−6466.
(12) Rajagopalan, R.; Tang, Y.; Ji, X.; Jia, C.; Wang, H. Advancements and Challenges in Potassium Ion Batteries: A Comprehensive Review. *Adv. Funct. Mater.* **2020**, *30*, No. 1909486.
(13) Eftekhari, A.; Jian, Z.; Ji, X. Potassium Secondary Batteries. *ACS Appl. Mater. Interfaces* **2017**, *9*, 4404−4419.
(14) Wu, Y.; Hu, S.; Xu, R.; Wang, J.; Peng, Z.; Zhang, Q.; Yu, Y. Boosting Potassium-Ion Battery Performance by Encapsulating Red Phosphorus in Free-Standing Nitrogen-Doped Porous Hollow Carbon Nanofibers. *Nano Lett.* **2019**, *19*, 1351−1358.
(15) Sankarasubramanian, S.; Kahky, J.; Ramani, V. Tuning Anion Solvation Energetics Enhances Potassium−Oxygen Battery Performance. *Proc. Natl. Acad. Sci. U. S. A.* **2019**, *116*, 14899.
(16) Qin, L.; Xiao, N.; Zheng, J.; Lei, Y.; Zhai, D.; Wu, Y. Localized High Concentration Electrolytes Boost Potassium Storage in High Loading Graphite. *Adv. Energy Mater.* **2019**, *9*, No. 1902618.
(17) Eftekhari, A. A Potassium Secondary Cell Based on Prussian Blue Cathode. *J. Power Sources* **2004**, *126*, 221−228.
(18) Lerf, A. Storylines in Intercalation Chemistry. *Dalton Trans.* **2014**, *43*, 10276−10291.
(19) Vaalma, C.; Giffin, G. A.; Buchholz, D.; Passerini, S. Non-Aqueous K-Ion Battery Based on LayeredK0.3MnO2 and Hard Carbon/Carbon Black. *J. Electrochem. Soc.* **2016**, *163*, A1295−A1299.
(20) Zhang, W.; Huang, W.; Zhang, Q. Organic Materials as Electrodes in Potassium-Ion Batteries. *Chem. − Eur. J.* **2021**, *27*, 6131−6144.
(21) Schon, T. B.; McAllister, B. T.; Li, P.-F.; Seferos, D. S. The Rise of Organic Electrode Materials for Energy Storage. *Chem. Soc. Rev.* **2016**, *45*, 6345−6404.
(22) Côté, A. P.; Benin, A. I.; Ockwig, N. W.; O'Keeffe, M.; Matzger, A. J.; Yaghi, O. M. Porous, Crystalline. Covalent Organic Frameworks. *Science* **2005**, *310*, 1166−1170.
(23) Wu, M.-X.; Yang, Y.-W. Applications of Covalent Organic Frameworks (COFs): From Gas Storage and Separation to Drug Delivery. *Chin. Chem. Lett.* **2017**, *28*, 1135−1143.
(24) Haug, W. K.; Moscarello, E. M.; Wolfson, E. R.; McGrier, P. L. The Luminescent and Photophysical Properties of Covalent Organic Frameworks. *Chem. Soc. Rev.* **2020**, *49*, 839−864.
(25) Sun, T.; Xie, J.; Guo, W.; Li, D.-S.; Zhang, Q. Covalent−OrganicFrameworks: Advanced Organic Electrode Materials for Rechargeble Batteries. *Adv. Energy Mater.* **2020**, *10*, No. 1904199.
(26) Xu, F.; Yang, S.; Chen, X.; Liu, Q.; Li, H.; Wang, H.; Wei, B.; Jiang, D. Energy-Storage Covalent Organic Frameworks: Improving Performance Via Engineering Polysulfide Chains on Walls. *Chem. Sci.* **2019**, *10*, 6001−6006.
(27) Haug, W. K.; Wolfson, E. R.; Morman, B. T.; Thomas, C. M.; McGrier, P. L. A Nickel-Doped Dehydrobenzoannulene-Based Two Dimensional Covalent Organic Framework for the Reductive Cleavage of Inert Aryl C-S Bonds. *J. Am. Chem. Soc.* **2020**, *142*, 5521−5525.
(28) Sharma, R. K.; Yadav, P.; Yadav, M.; Gupta, R.; Rana, P.; Srivastava, A.; Zbořil, R.; Varma, R. S.; Antonietti, M.; Gawande, M. B. Recent Development of Covalent Organic Frameworks (COFs): Synthesis and Catalytic (Organic-Electro-Photo) Applications. *Mater. Horiz.* **2020**, *7*, 411−454.
(29) Albacete, P.; López-Moreno, A.; Mena-Hernando, S.; Platero-Prats, A. E.; Pérez, E. M.; Zamora, F. Chemical Sensing of Water Contaminants by a Colloid of a Fluorescent Imine-Linked Covalent Organic Framework. *Chem. Commun.* **2019**, *55*, 1382−1385.
(30) Ascherl, L.; Evans, E. W.; Gorman, J.; Orsborne, S.; Bessinger, D.; Bein, T.; Friend, R. H.; Auras, F. Perylene-Based Covalent Organic Frameworks for Acid Vapor Sensing. *J. Am. Chem. Soc.* **2019**, *141*, 15693−15699.
(31) Gao, Q.; Li, X.; Ning, G.; Leng, K.; Tian, B.; Liu, C.; Tang, W.; Xu, H.; Loh, K. P. Highly Photoluminescent Two-Dimensional Imine Based Covalent Organic Frameworks for Chemical Sensing. *Chem. Commun.* **2018**, *54*, 2349−2352.
(32) Luo, Z.; Luojia, L.; Ning, J.; Lei, K.; Lu, Y.; Li, F.; Chen, J. A Microporous Covalent-Organic Framework with Abundant Accessible Carbonyl Groups for Lithium-Ion Batteries. *Angew. Chem., Int. Ed.* **2018**, *57*, 9443−9446.
(33) Lei, Z.; Yang, Q.; Xu, Y.; Guo, S.; Sun, W.; Liu, H.; Lv, L.; Zhang, Y.; Wang, Y. Boosting Lithium Storage in Covalent Organic Framework via Activation of 14-Electron Redox Chemistry. *Nat. Commun.* **2018**, *9*, 576.
(34) Wang, S.; Wang, Q.; Shao, P.; Han, Y.; Gao, X.; Ma, L.; Yuan, S.; Ma, X.; Zhou, J.; Feng, X.; Wang, B. Exfoliation of Covalent Organic Frameworks into Few-Layer Redox-Active Nanosheets as Cathode Materials for Lithium-Ion Batteries. *J. Am. Chem. Soc.* **2017**, *139*, 4258−4261.
(35) Chen, Z.; Zhang, H.; Ci, C.; Sun, W.; Wang, Y. Few-Layered Boronic Ester Based Covalent Organic Frameworks/Carbon Nanotube Composites for High-Performance K-Organic Batteries. *ACS Nano* **2019**, *13*, 3600−3607.
(36) Feriante, C. H.; Jhulki, S.; Evans, A. M.; Dasari, R. R.; Slicker, K.; Dichtel, W. R.; Marder, S. R. Rapid Synthesis of High Surface Area Imine-Linked 2D Covalent Organic Frameworks by Avoiding Pore Collapse During Isolation. *Adv. Mater.* **2020**, *32*, No. 1905776.
(37) Wolfson, E. R.; Xiao, N.; Schkeryantz, L.; Haug, W. K.; Wu, Y.; McGrier, P. L. A Dehydrobenzoannulene-Based Two-Dimensional Covalent Organic Framework as an Anode Material for Lithium-Ion Batteries. *Mol. Syst. Des. Eng.* **2020**, *5*, 97−101.
(38) Lei, Y.; Han, D.; Dong, J.; Qin, L.; Li, X.; Zhai, D.; Li, B.; Wu, Y.; Kang, F. Unveiling the Influence of Electrode/Electrolyte Interface on the Capacity Fading for Typical Graphite-Based Potassium-Ion Batteries. *Energy Storage Mater.* **2020**, *24*, 319−328.
(39) Kim, H.; Yoon, G.; Lim, K.; Kang, K. A. A Comparative Study of Graphite Electrodes using the Co-Intercalation Phenomenon for Rechargeable Li, Na and K Batteries. *Chem. Commun.* **2016**, *52*, 12618−12621.
(40) The charge and discharge voltage profiles (V vs K^+/K) for DBA-COF 3 and TAEB-COF are provided in Fig. S19 & S23, respectively, in the ESI.
(41) Li, S.-Y.; Li, W.-H.; Wu, X.-L.; Tian, Y.; Yue, J.; Zhu, G. Pore-Size Dominated Electrochemical Properties of Covalent Triazine Frameworks as Anode Materials for K-ion Batteries. *Chem. Sci.* **2019**, *10*, 7695−7701.
(42) Maier, W. F.; Lau, G. C.; McEwen, A. B. Effect of Bending on the Reactivity of Alkynes: A Semiempirical Study. *J. Am. Chem. Soc.* **1985**, *107*, 4724−4731.
(43) Chen, G.; Yao, X.; Cao, Q.; Ding, S.; He, J.; Wang, S. Flexible Free-standing SnS_2/Carbon Nanofibers Anode for High Performance Sodium-Ion Batteries. *Mater. Lett.* **2019**, *234*, 121−124.
(44) Yan, Y.; Ma, Z.; Lin, H.; Rui, K.; Zhang, Q.; Wang, Q.; Du, M.; Li, D.; Zhang, Y.; Zhu, J.; Huang, W. Hydrogel Self-Templated Synthesis of $Na_3V_2(PO_4)3$@C@CNT Porous Network as Ultrastable Cathode for Sodium-Ion Batteries. *Compos. Commun.* **2019**, *13*, 97−102.
(45) Wang, H.; Zhai, D.; Kang, F. Solid Electrolyte Interphase (SEI) in Potassium Ion Batteries. *Energy Environ. Sci.* **2020**, *13*, 4583−4608.

https://doi.org/10.1021/acsami.1c10870
ACS Appl. Mater. Interfaces 2021, 13, 41628−41636